Optical Engineering

OpticalEngineering.SPIEDigitalLibrary.org

Nondestructive evaluation of low-velocity impact-induced damage in basalt-carbon hybrid composite laminates using eddy current-pulsed thermography

Hai Zhang
Stefano Sfarra
Ahmad Osman
Fabrizio Sarasini
Udo Netzelmann
Bernd Valeske
Nicolas P. Avdelidis
Clemente Ibarra-Castanedo
Xavier Maldague

SPIE.

Hai Zhang, Stefano Sfarra, Ahmad Osman, Fabrizio Sarasini, Udo Netzelmann, Bernd Valeske, Nicolas P. Avdelidis, Clemente Ibarra-Castanedo, Xavier Maldague, "Nondestructive evaluation of low-velocity impact-induced damage in basalt-carbon hybrid composite laminates using eddy current-pulsed thermography," *Opt. Eng.* **58**(4), 041602 (2018), doi: 10.1117/1.OE.58.4.041602.

Nondestructive evaluation of low-velocity impact-induced damage in basalt-carbon hybrid composite laminates using eddy current-pulsed thermography

Hai Zhang,[a,b,*,†] Stefano Sfarra,[c,d] Ahmad Osman,[b,e] Fabrizio Sarasini,[f] Udo Netzelmann,[b] Bernd Valeske,[b,e] Nicolas P. Avdelidis,[a,g] Clemente Ibarra-Castanedo,[a] and Xavier Maldague[a]

[a]Laval University, Department of Electrical and Computer Engineering, Computer Vision and Systems Laboratory (CVSL), Quebec City, Canada
[b]Fraunhofer-Institute for Nondestructive Testing IZFP, Department of Inspection of Components and Assemblies, Saarbruecken, Germany
[c]University of L'Aquila, Department of Industrial and Information Engineering and Economics, L'Aquila, Italy
[d]Tomsk Polytechnic University, Tomsk, Russia
[e]University of Applied Sciences Saarland, htw saar, Saarbruecken, Germany
[f]Sapienza University of Rome, Department of Chemical Engineering Materials Environment and UDR INSTM, Rome, Italy
[g]Aerospace Integration Research Centre (AIRC), Cranfield, United Kingdom

Abstract. Recently, basalt-carbon hybrid composite structures have attracted increasing attention due to their better damage tolerance, if compared with carbon fiber-reinforced polymer composites (CFRP). Low-velocity is considered as one of the most severe threats to composite materials as it is usually invisible and it occurs frequently in service. With this regard, nondestructive testing (NDT) techniques, especially emerging modalities, are expected to be an effective damage detection method. Eddy current-pulsed thermography (ECPT), as an emerging NDT technique, was used to evaluate the damage induced by low-velocity impact loading in a CFRP laminate, as well as in two different-structured basalt-carbon hybrid composite laminates. In addition, ultrasonic C-scan and x-ray computed tomography were performed to validate the thermographic results. Pulsed phase thermography, principal component thermography, and partial least squares thermography were used to process the thermal data and to retrieve the damage imagery. Then, a further analysis was performed on the imagery and temperature profile. As a result, it is concluded that ECPT is an effective technique for hybrid composite evaluation. The impact energy tends to create an interlaminar damage in a sandwich-like structure, while it tends to create an intralaminar damage in an intercalated stacking structure. [DOI: 10.1117/1.OE.58.4.041602]

Keywords: eddy current pulsed thermography; composite; basalt; carbon; nondestructive testing.

Paper 180534SS received Apr. 12, 2018; accepted for publication Sep. 11, 2018; published online Oct. 27, 2018.

1 Introduction

Due to the features of high strength, high stiffness, and low weight, carbon fiber-reinforced polymer (CFRP) has been widely used as an alternative material to aluminum alloy in many industrial applications such as in the aerospace industry.[1,2] However, CFRP still has weaknesses that limit its wider use, e.g., its low toughness, which leads to its weak damage-resistance capability.[3–5] A possible solution to compensate this weakness is fiber hybridization.[6] Carbon fibers are usually hybridized with high toughness fibers to obtain a better damage tolerance.[7–10] In this aspect, glass fiber has been used for this purpose in the last decade, which has been proved to be efficacious.[11–14] However, the manufacturing of glass fiber may lead to the contamination of the environment, and its disposal at the end of life is also a difficult problem.[15] In this consideration, basalt fiber has attracted increasing attention due to its eco-friendly feature as well as its inexpensive price.[16–18]

A few reports have focused on the study of mechanical behaviors of hybrid composite structures in the open literature.[19–21] However, nondestructive evaluation (NDE) has not been widely reported on this topic. Recently, the authors used traditional NDE techniques including optical and mechanical excitation thermography to fulfill this field.[22,23] These works studied the optical and mechanical thermographic evaluation on basalt-carbon hybrid composite laminates subjected to both ballistic and low-velocity impact loadings. This study gave promising scientific outcomes; however, more emerging NDE techniques are expected to be used in this study, e.g., laser-based thermography,[24] eddy current thermography,[25–28] air-coupled ultrasound,[29] and terahertz imaging.[30–33] In this consideration, the authors reported a study on the evaluation of ballistic impact damage in basalt-carbon hybrid composite panels more recently.[34] This study was based on an emerging eddy current pulsed thermography (ECPT) technique. However, an in-depth study of ECPT on the damage induced by low-velocity impact loadings has not been documented yet. If compared with ballistic impact damage, low-velocity impact damage is a more severe threat to aircraft safety, as it is usually invisible and it occurs frequently in service.[35–37] Accordingly, nondestructive testing (NDT) has more practical meaning for the evaluation of low-velocity impact damage in hybrid composite materials.

In this paper, ECPT was used to evaluate the damage induced by low-velocity impact loading in a CFRP laminate,

*Address all correspondence to: Hai Zhang, E-mail: hai.zhang.1@ulaval.ca

†Current address: Department of Mechanical and Industrial Engineering, University of Toronto, Toronto, M5S 3G8, Canada

0091-3286/2018/$25.00 © 2018 SPIE

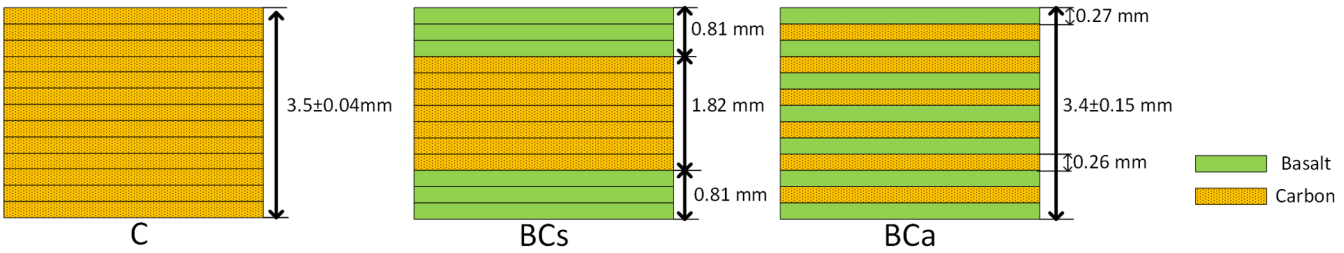

Fig. 1 Schematic stacking sequences of the specimens.

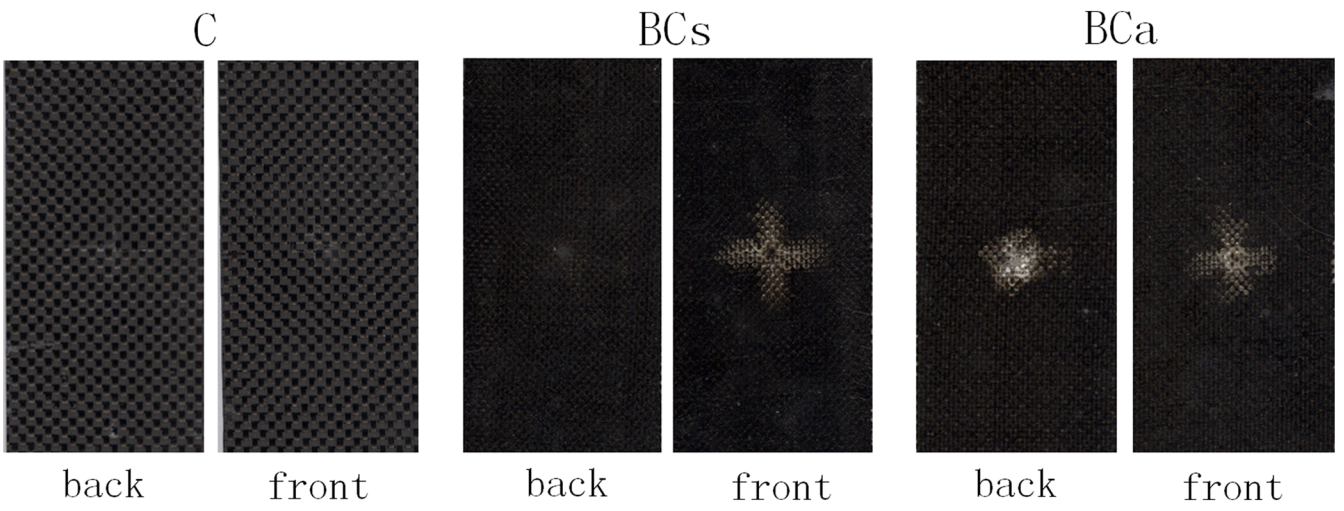

Fig. 2 Photographs of the specimens from both surfaces.

as well as in two different-structured basalt-carbon hybrid composite laminates. More specifically, intercalated stacking (BCa) and sandwich-like (BCs) structured hybrid specimens were used for the study. The impact energy of 12.5 J was used for the evaluation of the impact damage level. In addition, ultrasonic testing (UT) and x-ray computed tomography (CT) were also performed for the validation purpose. Due to the important role played by advanced image processing techniques, pulsed phase thermography (PPT), principal component thermography (PCT), and partial least squares thermography (PLST) were used herein showing a satisfactory computational performance. Then, a further analysis was performed on the basis of the imagery and temperature profile. Finally, the advantages and disadvantages of ECPT and of the different hybrid structures were analyzed for their potential industrial applications.[38]

2 Specimens

Figure 1 shows the schematic diagram of the BCs and BCa structures. BCs was stacked as a sandwich structure with seven carbon fiber layers (as the core) and three basalt fiber layers for each side (as the skins). BCa has seven basalt fiber layers and six carbon fiber layers alternatively stacked to keep basalt plies as the outer layers on both sides. In addition, a CFRP (C) laminate was also manufactured as a reference specimen for comparative purposes. A basalt fiber-reinforced polymer (BFRP) composite specimen was not introduced in this paper as basalt fiber is insulating and therefore, eddy current will not be created in a BFRP laminate.

A falling dart impact machine was used to impact the specimens at 12.5 J by keeping the indenter mass (6.929 kg) constant with a hemispherical impactor head (12.7 mm of diameter). The circular specimen holder has an external diameter of 60 mm and inner diameter of 40 mm.

Figure 2 shows the photographs of all the specimens from both surfaces. These specimens have a dimension of 180 mm × 60 mm, and their thickness is ∼3.5 mm (see Fig. 1). The CFRP specimen shows a penetration of the dart through the thickness with splitting due to its brittle nature. The BCs specimen shows a damage without backsurface splitting. The BCa specimen shows an intermediate damage pattern with respect to the CFRP and the BCs specimens. In particular, a bulge is present on the surface of BCa.

3 Methodology

3.1 *Experiments*

Figure 3 shows the schematic configuration of the ECPT experimental system used in this paper. The induction heater (7 kW) creates a pulse excitation signal (150 kHz, 0.2 s duration), which includes a period of high-frequency alternating current having high amplitude. The current is then driven into an inductive coil (5 cm × 5 cm) positioned on the front side of the specimen with a minor distance. An infrared camera FLIR SC5000 (320 × 256 pixels, 150 fps) was used to record the temperature profile (2 s of recording time).

ECPT involves interactions of electromagnetic and thermal behaviors, which include the induced eddy current, Joule heating, and heat conduction.[39]

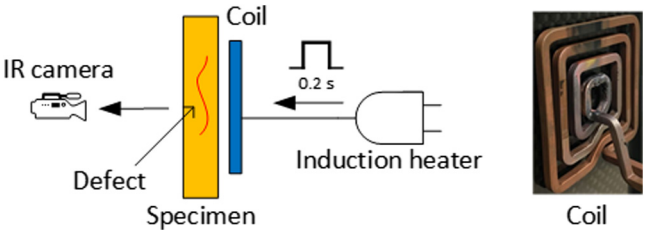

Fig. 3 Schematic configuration of the ECPT experimental system.

When the current passes through the coil, it generates an eddy current. The eddy current is in respect to a subsurface penetration depth δ, which corresponds to the exponentially dampened skin effect, described as follows:

$$\delta = (\pi\mu\sigma f)^{-1/2}, \tag{1}$$

where f is the excitation frequency, σ is the electrical conductivity, and μ is the magnetic permeability.[40]

The temperature of material increases because of resistible heating from the generated eddy current (Joule heating), which is described as follows:

$$Q = \frac{1}{\sigma}|J_s|^2 = \frac{1}{\sigma}|\sigma E|^2, \tag{2}$$

where Q is the sum of the generated energy, J_s is the eddy current density, and E is the electric field density.[40]

For hybrid specimens, thermal diffusion behavior is more complex and it is dependent on the specimen structures due to the fact that carbon fiber is conductive, but basalt fiber is insulating.

3.2 *Infrared Image Processing*

3.2.1 *Pulse phase thermography*

PPT[41] can be used for quantitative analysis in a straightforward manner by extracting amplitude and phase images using Fourier transform (FT). In PPT, phase is usually more useful than amplitude, as it can retrieve a deeper depth. Moreover, phase is less affected by environmental reflections, emissivity variations, nonuniform heating, surface geometry, and orientation.[42]

3.2.2 *Principal component thermography*

PCT[43] can extract image characteristics and it reduces undesirable signals. PCT relies on singular value decomposition, which extracts spatial and temporal data from a matrix in a compact manner by projecting original data onto empirical orthogonal functions. In addition, PCT is also suitable to be combined with other image processing techniques.[44–46]

3.2.3 *Partial least squares thermography*

PLST[47] is a statistical correlation algorithm based on partial least squares regression. It computes loading and score vectors, which are correlated to the predicted block. The block describes a large amount of variations in a predictor matrix, which corresponds to the obtained surface temperature profile.

4 Result Analysis

Figure 4 shows the UT imagery results of all of the specimens. A 64 elements of phased-array ultrasonic probe, which has a frequency of 2.25 MHz, was used in the experiments. The scale bar corresponds to the ultrasonic signal reflection rate.

In Fig. 4, it can be observed that the damage induced by the low-velocity impact can be clearly seen (the colors of dark blue and white, which correspond to a bare signal reflection). The CFRP specimen shows the most concentrated damaged area, whereas the BCs specimen has the most extended damaged area. This phenomenon illustrates that the absorbed energy E_a tends to create a through-thickness splitting damage in the CFRP specimen due to its inherent limited ductility, while E_a tends to be converted into an extended delaminated area in the BCs specimen due to its lower interlaminar shear strength.

The damaged area in the BCa specimen is between the CFRP and the BCs specimens as shown in Fig. 4. This is because BCa has an intermediate impact-resistance mechanical behavior, if compared with the CFRP and BCs structure. Moreover, the back-side inspection results show a higher extended area and a lower signal reflection rate. This indicates that the impact damage is closer to the back surface of the impact. Finally, it is worth emphasizing that the cross-shape (see Fig. 2) is difficult to identify using ultrasonic C-scan due to the fact that the ultrasonic signals

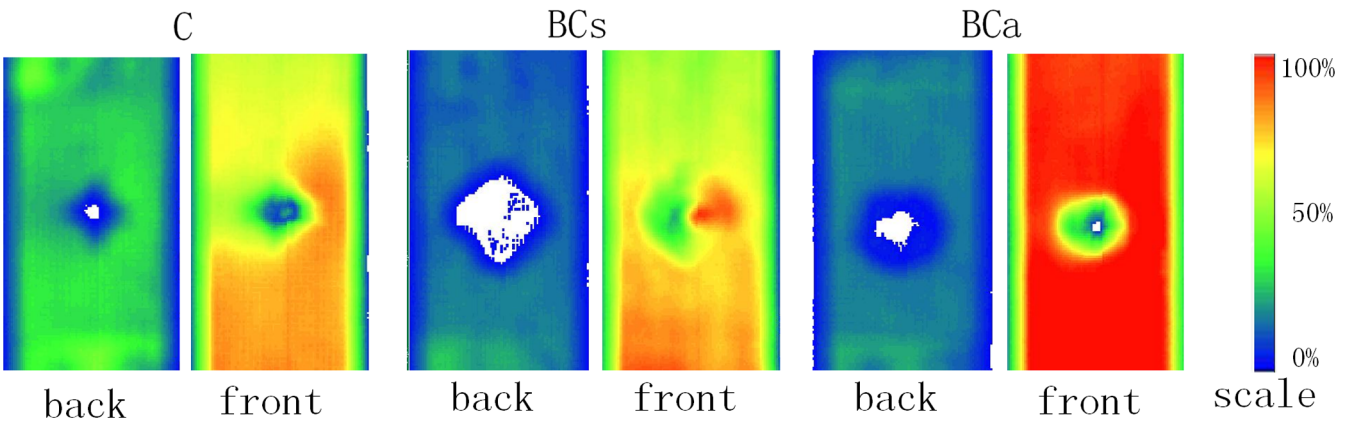

Fig. 4 Ultrasonic C-scan imagery from both inspection surfaces.

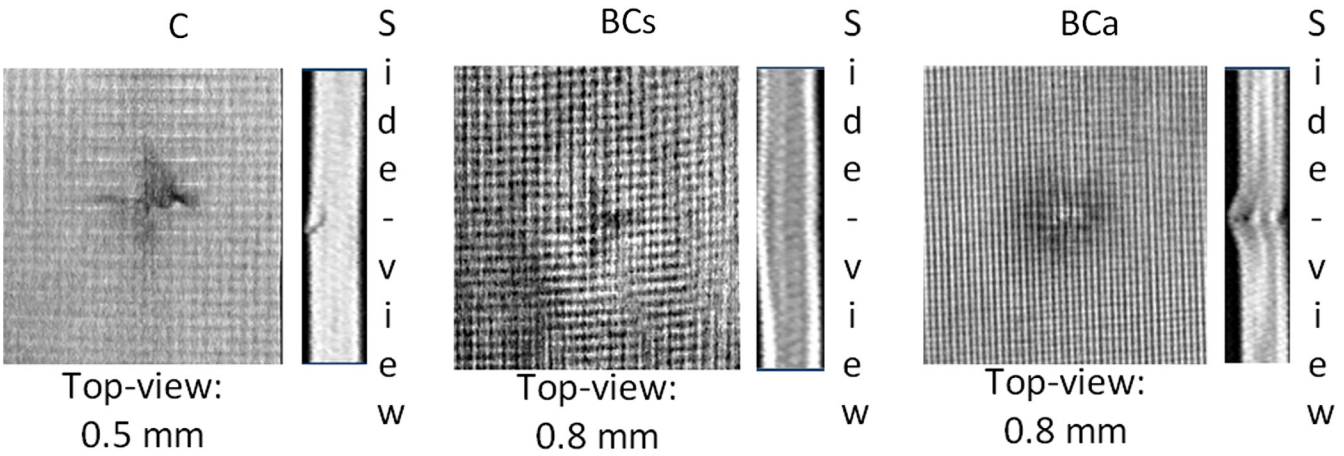

Fig. 5 CT slices of the specimens from both top-view and side-view inspections.

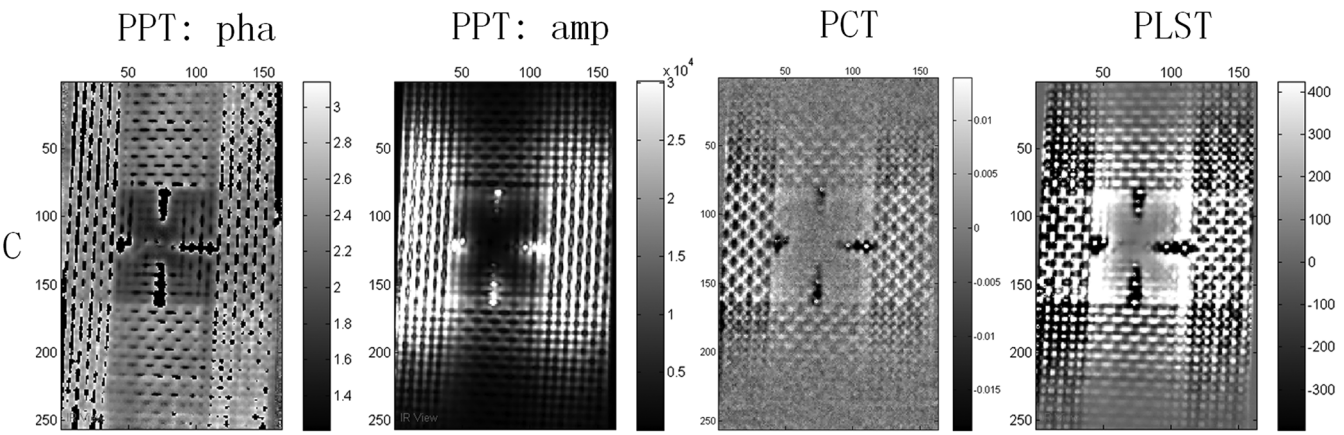

Fig. 6 ECPT imagery results of the CFRP specimen after image processing.

were disturbed on the locations of both penetrated-like and delaminated areas.

Figure 5 shows the CT slices of the specimens from both top-view and side-view inspections. The applied system has a spatial resolution of 100 μm. In Fig. 5, darker colors represent low-density areas, whereas brighter colors represent high-density areas. From top-view inspections, it can be observed that the CT slices have a higher spatial resolution than UT. Therefore, it is easier to detect fiber preforms using CT as shown in Fig. 5. On the contrary, these fibers are difficult to detect using UT (see Fig. 4).

Indeed, CT shows a few advantages over UT, but usually it has a lower imagery contrast than UT. Accordingly, it is more difficult to determine the damaged areas using CT than UT. In Fig. 5, CT can show the cross-shaped splitting-like damage in both CFRP and hybrid specimens, but it cannot be observed using UT as discussed previously.

In Fig. 5, side-view inspections provide promising additional clues for the interpretation of UT results: impact energy E_a tends to create a through-thickness splitting damage in CFRP specimen, as it has an inherent limited ductility. On the contrary, E_a tends to be converted into an interlaminar delaminated damage in BCs specimens because the latter has a lower interlaminar shear strength. The damaged feature in BCa is between the CFRP and BCs structure, as it has an intermediate impact resistance mechanical behavior. It can be summarized that UT and CT have different advantages and, therefore, both of them were used as referenced techniques for comparative purposes in this paper.

Figure 6 shows the ECPT imagery results of the CFRP specimen after infrared image processing. In ECPT, eddy currents are created in carbon fibers due to their conductivity. Accordingly, the fibers have higher temperatures than resin. This fact results in the phenomenon that fibers have brighter colors in the imagery results as shown in Fig. 6. In the PPT-amplitude result, the cross-shaped damage is brighter because more eddy currents excessively exist in this crack-like area. Different from fibers, the cross-shaped damage is darker in PPT-phase, PCT, and PLST postprocessed results, because these image processing methods retrieved its time-domain evolution, which departs from the near-straight-line behavior.

In Fig. 6, it can be observed that the cross-shaped penetrated-like damage can be clearly detected in all of the imagery results, which were obtained from different image processing methods. Moreover, ECPT clearly shows the cross-shaped damage around the impacted areas, and its imagery contrast is over CT. In addition, the fiber preforms can also be detected in ECPT with a higher contrast than CT, which is shown in Fig. 5.

Figure 7 shows the temperature profile of the CFRP specimen. In Fig. 7, the measuring unit of the IR camera is

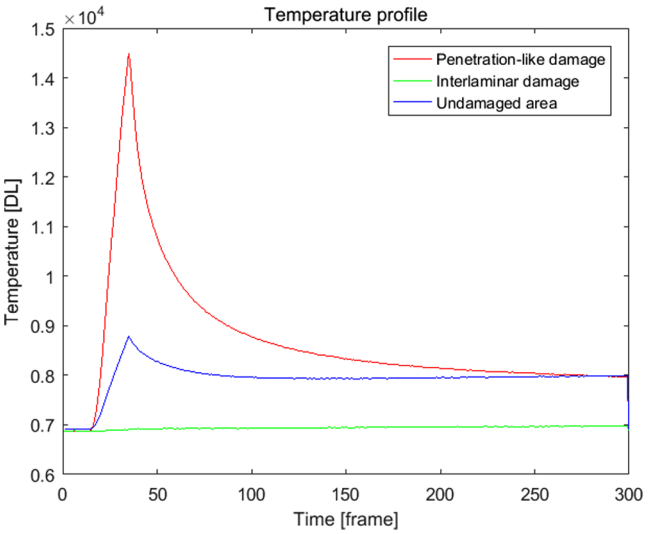

Fig. 7 Temperature profile of the CFRP specimen.

digital level (DL). Presenting results in units of DL is common in the community because the parameter of interest in active thermography is only temperature changes. If a course estimation of the temperature rise is needed, it is usually calculated 1 K for 50 DL.

In Fig. 7, it can be obversed that the cross-shaped damage shows a higher temperature, while the intralaminar damage shows a lower temperature. This coincides with the imagery results in Fig. 6, in which the intralaminar damage area shows a lower temperature in the format of a darker color.

In ECPT, the cross-shaped penetrated-like damage shows a thermal behavior similar to that of cracks, and it also shows an imagery feature similar to that of cracks as shown in Fig. 6. Finally, it is worth emphasizing that the temperature profile in the CFRP specimen shows a significant heating-up and cooling-down curve, which is obviously different from the hybrid structured specimens discussed below.

Figure 8 shows the ECPT imagery results of the BCs and BCa specimens. The cross-shaped damage can be detected in the BCs specimen, but it is barely visible in the BCa specimen. The PPT-phase result shows more identifications for the cross-shaped damage, if compared with other image processing methods. This is because phase imagery is less affected by surrounding noise.

Interestingly, the BCs specimen exhibits a more extensive damaged area, as the interlaminar delaminated damage in the BCs specimen is more detectable than in the BCa specimen. This phenomenon is in agreement with the referenced UT and CT inspections as shown in Figs. 4 and 5. This is also explained in the above-mentioned sections.

In Fig. 8, ECPT highlights the intralaminar damage in the BCa specimen in a similar manner as those observed in the CFRP specimen, also in agreement with the referenced UT and CT inspections in Figs. 4 and 5. This confirms the validity of the previous assessment that the impact resistance mechanical behavior of the BCa specimen is more similar to that of the CFRP specimen when compared with the BCs structured specimen.

Figures 9 and 10 show the temperature profiles of the BCs and BCa specimens. It should be emphasized that a significant temperature cooling-down evolution is observed in

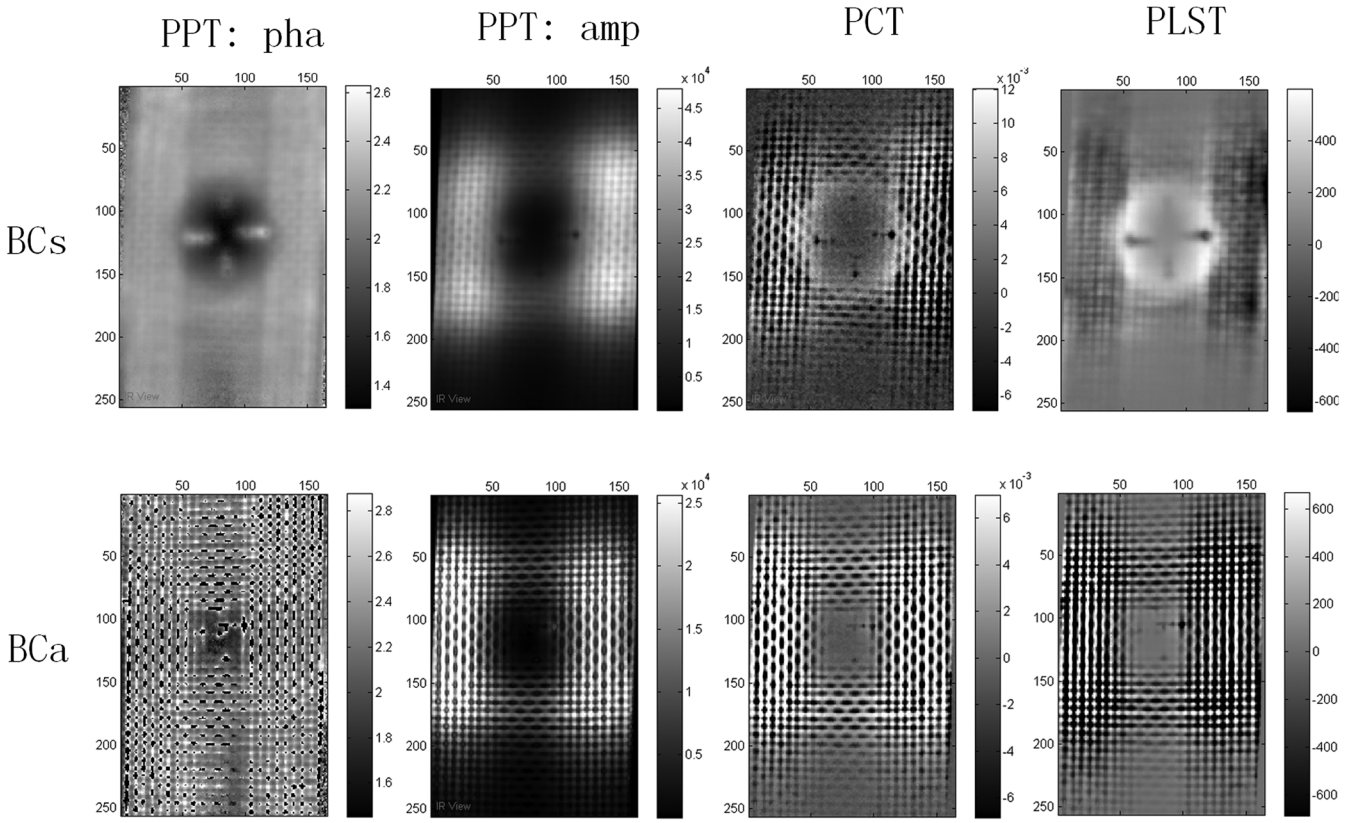

Fig. 8 ECPT imagery results of the hybrid specimens after image processing.

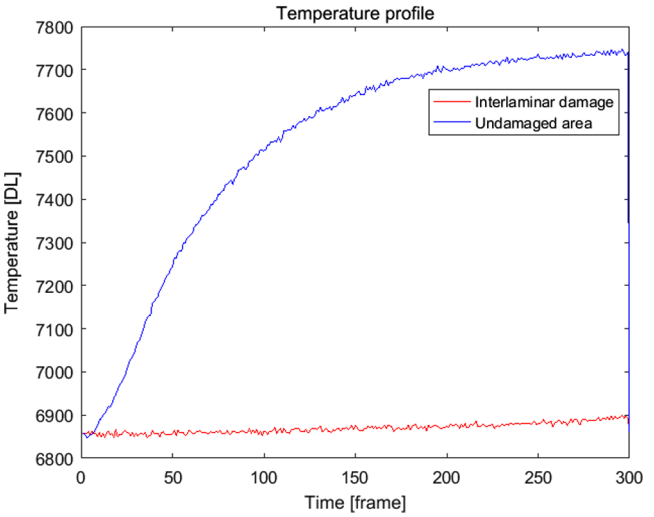

Fig. 9 Temperature profile of the BCs specimen.

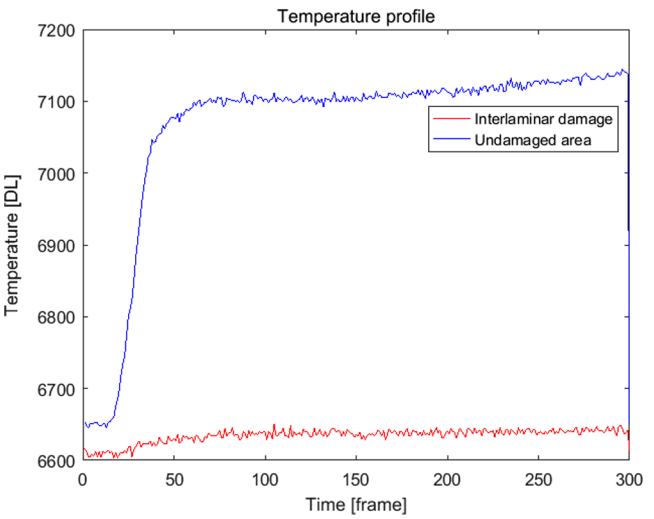

Fig. 10 Temperature profile of the BCa specimens.

neither the BCs nor BCs specimen. On the contrary, a significant cooling-down curve can be clearly observed in the CFRP specimen, as discussed previously (see Fig. 7). This is due to the fact that basalt fibers are insulating and they are formatted into the skinned surface layers. Thus, eddy currents are generated only in subskinned carbon fibers. Therefore, surface layers made of basalt fibers and resins show only a temperature diversification. This temperature diversification is diffused from neighboring conductive subsurface carbon fibers. BCs shows a smoother temperature evolution when compared with BCa. This is a proof for this conclusion, as BCs has a thicker insulating skinned layer than BCa.

5 Conclusions

ECPT is an effective technique that can be used to evaluate the damage induced by low-velocity impact loading in both CFRP and hybrid composite structures. The ECPT imagery results were validated by and compared with UT and CT. Interestingly, ECPT showed a higher imagery contrast and it also provided a higher spatial resolution. Therefore, ECPT can be considered as an emerging *in situ* NDT technique for industrial inspection of hybrid composite products.

In addition, it was analyzed that impact energy E_a tended to create an interlaminar delaminated damage in BCs structure, while it tended to create an intralaminar penetration-like damage in BCa structure. Infrared image processing methods used in this paper, including PPT, PCT and PLST, contributed to the understanding of the above-mentioned summary. More cutting-edge infrared image processing methods[48] and modeling simulations[49] are expected in order to understand more about the ECPT mechanism and mechanical impact behavior in future work.

Acknowledgments

This research was supported by the Canada Research Chair in Multipolar Infrared Vision (MiViM) and the Natural Sciences and Engineering Research Council (NSERC) Canada through a Discovery Grant. This research is also supported by the Fonds de recherche du Québec-Nature et technologies (FRQNT) and the Regroupement pour l'étude des environnements partagés intelligents répartis (REPARTI) through the International Internship Program (no. 211450).

References

1. C. Meeks, E. Greenhalgh, and B. G. Falzon, "Stiffener debonding mechanisms in post-buckled CFRP aerospace panels," *Compos. Part A* **36**(7), 934–946 (2005).
2. H. Zhang et al., "Optical excitation thermography for twill/plain weaves and stitched fabric dry carbon fibre preform inspection," *Compos. Part A* **107**, 282–293 (2018).
3. M. Arai et al., "Mode I and mode II interlaminar fracture toughness of CFRP laminates toughened by carbon nanofiber interlayer," *Compos. Sci. Technol.* **68**(2), 516–525 (2008).
4. J. Kim et al., "Fracture toughness of CFRP with modified epoxy resin matrices," *Compos. Sci. Technol.* **43**(3), 283–297 (1992).
5. N. Sela, O. Ishai, and L. Banks-Sills, "The effect of adhesive thickness on interlaminar fracture toughness of interleaved CFRP specimens," *Composites* **20**(3), 257–264 (1989).
6. M. Jalalvand, G. Czél, and M. R. Wisnom, "Damage analysis of pseudo-ductile thin-ply UD hybrid composites—a new analytical method," *Compos. Part A* **69**, 83–93 (2015).
7. M. Hosur, M. Adbullah, and S. Jeelani, "Studies on the low-velocity impact response of woven hybrid composites," *Compos. Struct.* **67**(3), 253–262 (2005).
8. E. Sevkat et al., "Drop-weight impact of plain-woven hybrid glass–graphite/toughened epoxy composites," *Compos. Part A* **40**(8), 1090–1110 (2009).
9. M. M. Thwe and K. Liao, "Durability of bamboo-glass fiber reinforced polymer matrix hybrid composites," *Compos. Sci. Technol.* **63**(3), 375–387 (2003).
10. J. Gustin et al., "Low velocity impact of combination Kevlar/carbon fiber sandwich composites," *Compos. Struct.* **69**(4), 396–406 (2005).
11. S. S. Cheon et al., "Impact energy absorption characteristics of glass fiber hybrid composites," *Compos. Struct.* **46**(3), 267–278 (1999).
12. N. Naik et al., "Impact response and damage tolerance characteristics of glass–carbon/epoxy hybrid composite plates," *Compos. Part B* **32**(7), 565–574 (2001).
13. H. Yu et al., "Pseudo-ductility in intermingled carbon/glass hybrid composites with highly aligned discontinuous fibres," *Compos. Part A* **73**, 35–44 (2015).
14. G. Czél and M. Wisnom, "Demonstration of pseudo-ductility in high performance glass/epoxy composites by hybridisation with thin-ply carbon prepreg," *Compos. Part A* **52**, 23–30 (2013).
15. A. Ross, "Basalt fibers: alternative to glass?," *Compos. Technol.* **12**(4), 44–48 (2006).
16. R. Petrucci et al., "Impact and post-impact damage characterisation of hybrid composite laminates based on basalt fibres in combination with flax, hemp and glass fibres manufactured by vacuum infusion," *Compos. Part B* **69**, 507–515 (2015).
17. T. Deák and T. Czigány, "Chemical composition and mechanical properties of basalt and glass fibers: a comparison," *Textile Res. J.* **79**(7), 645–651 (2009).
18. A. Dorigato and A. Pegoretti, "Fatigue resistance of basalt fibers-reinforced laminates," *J. Compos. Mater.* **46**(15), 1773–1785 (2012).

19. F. Sarasini et al., "Drop-weight impact behaviour of woven hybrid basalt-carbon/epoxy composites," *Compos. Part B* **59**, 204–220 (2014).
20. M. Kim et al., "Effects of silane-modified carbon nanotubes on flexural and fracture behaviors of carbon nanotube-modified epoxy/basalt composites," *Compos. Part B* **43**(5), 2298–2302 (2012).
21. T. Czigány, "Special manufacturing and characteristics of basalt fiber reinforced hybrid polypropylene composites: mechanical properties and acoustic emission study," *Compos. Sci. Technol.* **66**(16), 3210–3220 (2006).
22. S. Sfarra et al., "Analysis of damage in hybrid composites subjected to ballistic impacts: an integrated non-destructive approach," in *Handbook of Composites from Renewable Materials, Physico-Chemical and Mechanical Characterization*, V. K. Thakur, M. K. Thakur, and M. R. Kessler, Eds., pp. 175–210, John Wiley & Sons (2017).
23. H. Zhang et al., "Optical and mechanical excitation thermography for impact response in basalt-carbon hybrid fiber-reinforced composite laminates," *IEEE Trans. Ind. Inf.* **14**(2), 514–522 (2018).
24. H. Zhang et al., "An experimental and analytical study of micro-laser line thermography on micro-sized flaws in stitched carbon fiber reinforced polymer composites," *Compos. Sci. Technol.* **126**, 17–26 (2016).
25. Y. He and R. Yang, "Eddy current volume heating thermography and phase analysis for imaging characterization of interface delamination in CFRP," *IEEE Trans. Ind. Informatics* **11**(6), 1287–1297 (2015).
26. Y. He et al., "Volume or inside heating thermography using electromagnetic excitation for advanced composite materials," *Int. J. Therm. Sci.* **111**, 41–49 (2017).
27. B. Gao et al., "Multidimensional tensor-based inductive thermography with multiple physical fields for offshore wind turbine gear inspection," *IEEE Trans. Ind. Electron.* **63**(10), 6305–6315 (2016).
28. B. Gao et al., "Physics-based image segmentation using first order statistical properties and genetic algorithm for inductive thermography imaging," *IEEE Trans. Image Process.* **27**(5), 2160–2175 (2018).
29. H. Zhang et al., "A novel optical air-coupled ultrasound NDE sensing technique compared with infrared thermographic NDT on impacted composite materials," *Proc. SPIE* **10661**, 106610X (2018).
30. H. Zhang et al., "Non-destructive investigation of paintings on canvas by continuous wave terahertz imaging and flash thermography," *J. Nondestr. Eval.* **36**(2), 34 (2017).
31. K. Ahi, "Mathematical modeling of THz point spread function and simulation of THz imaging systems," *IEEE Trans. Terahertz Sci. Technol.* **7**(6), 747–754 (2017).
32. K. Ahi, S. Shahbazmohamadi, and N. Asadizanjani, "Quality control and authentication of packaged integrated circuits using enhanced-spatial-resolution terahertz time-domain spectroscopy and imaging," *Opt. Lasers Eng.* **104**, 274–284 (2018).
33. K. Ahi, "A method and system for enhancing the resolution of terahertz imaging," *Measurement* (2018).
34. H. Zhang et al., "Eddy current pulsed thermography for ballistic impact evaluation in basalt-carbon hybrid composite panels," *Appl. Opt.* **57**(18), D74–D81 (2018).
35. W. Cantwell and J. Morton, "The impact resistance of composite materials—a review," *Composites* **22**(5), 347–362 (1991).
36. M. Aktaş et al., "An experimental investigation of the impact response of composite laminates," *Composite Struct.* **87**(4), 307–313 (2009).
37. J. Wang, A. M. Waas, and H. Wang, "Experimental and numerical study on the low-velocity impact behavior of foam-core sandwich panels," *Composite Struct.* **96**, 298–311 (2013).
38. H. Zhang et al., "Nondestructive evaluation using eddy current pulsed thermographic imaging of basalt-carbon hybrid fiber-reinforced composite laminates subjected to low-velocity impact loadings," *Proc. SPIE* **10601**, 106010B (2018).
39. B. Gao et al., "Variational bayesian sub-group adaptive sparse component extraction for diagnostic imaging system," *IEEE Trans. Ind. Electron.* **65**(10), 8142–8152 (2018).
40. B. Gao et al., "Unsupervised sparse pattern diagnostic of defects with inductive thermography imaging system," *IEEE Trans. Ind. Inf.* **12**(1), 371–383 (2016).
41. X. Maldague and S. Marinetti, "Pulse phase infrared thermography," *J. Appl. Phys.* **79**(5), 2694–2698 (1996).
42. C. Ibarra-Castanedo and X. P. Maldague, "Infrared thermography," in *Handbook of Technical Diagnostics*, H. Czichos, Ed., pp. 175–220, Springer (2013).
43. N. Rajic, "Principal component thermography for flaw contrast enhancement and flaw depth characterisation in composite structures," *Composite Struct.* **58**(4), 521–528 (2002).
44. B. Yousefi et al., "Comparative analysis on thermal non-destructive testing imagery applying candid covariance-free incremental principal component thermography (CCIPCT)," *Infrared Phys. Technol.* **85**, 163–169 (2017).
45. H. Zhang et al., "An infrared-induced terahertz imaging modality for foreign object detection in a lightweight honeycomb composite structure," *IEEE Trans. Ind. Inf.* **14**(12), (2018).
46. B. Yousefi et al., "Comparison assessment of low rank sparse-PCA based-clustering/classification for automatic mineral identification in long wave infrared hyperspectral imagery," *Infrared Phys. Technol.* **93**, 103–111 (2018).
47. F. Lopez et al., "Optimization of pulsed thermography inspection by partial least-squares regression," *NDT E. Int.* **66**, 128–138 (2014).
48. B. Yousefi et al., "Continuum removal for ground based LWIR hyperspectral infrared imagery applying non-negative matrix factorization," *Appl. Opt.* **57**(21), 6219–6228 (2018).
49. H. Zhang et al., "Impact modelling and a posteriori non-destructive evaluation of homogeneous particleboards of sugarcane bagasse," *J. Nondestr. Eval.* **37**(1), 6 (2018).

Biographies for the authors are not available.